Wadas, S., Tschache, S., Polom, U., Krawczyk, C. (2020): Ground instability of sinkhole areas indicated by elastic moduli and seismic attributes. - Geophysical Journal International, 222, 1, 289-304.

https://doi.org/10.1093/gji/ggaa167

Geophysical Journal International

Geophys. J. Int. (2020) **222,** 289–304
Advance Access publication 2020 April 20
GJI General Geophysical Methods

doi: 10.1093/gji/ggaa167

Ground instability of sinkhole areas indicated by elastic moduli and seismic attributes

S.H. Wadas [1], S. Tschache,[2,3] U. Polom[1] and C.M. Krawczyk[4,5]

[1] *Leibniz Institute for Applied Geophysics, Stilleweg* 2, 30655 *Hannover, Germany. E-mail: sonja.wadas@leibniz-liag.de*
[2] *formerly Leibniz Institute for Applied Geophysics, Stilleweg* 2, 30655 *Hannover, Germany*
[3] *now University of Bergen, Department of Earth Science, Allégaten* 41, 5007 *Bergen, Norway*
[4] *GFZ German Research Centre for Geosciences, Telegrafenberg,* 14473 *Potsdam, Germany*
[5] *Technical University Berlin, Ernst-Reuter-Platz* 1, 10587 *Berlin, Germany*

Accepted 2020 April 3. Received 2020 April 3; in original form 2019 August 28

SUMMARY

Elastic moduli derived from vertical seismic profiles (VSPs) and 2-D S_H-wave reflection seismic profiles are used to characterize mechanical properties of rocks in sinkhole areas. V_P and V_S were used to calculate the Poisson's ratio and the dynamic shear modulus. The study shows that 2-D shear wave reflection seismics is suited to depict the heterogeneities of the subsurface induced by subsurface erosion. Low shear wave velocities of *ca*. 120–350 m s^{-1} and low shear strength values between 25 and 250 MPa are identified for the subsurface erosion horizon that consists of soluble Permian evapourites and the disturbed overlying deposits. These low values are a result of cavities and fractures induced by dissolution, creating unstable zones. In compliance with the shear modulus the Poisson's ratio derived from the VSPs shows values of 0.38–0.48 for both the presumed subsurface erosion horizon, and the deposits above. This is a further indicator of reduced underground stability. In the VSPs, anomalies of the shear modulus and the Poisson's ratio correlate with low electrical resistivities of less than 10 Ωm from borehole logs, indicating high conductivity due to fluid content. Further investigation reveals a conversion of *S*-to-*P* wave for the subsurface erosion horizon, which is probably the result of dipping layers and an oriented fracture network. Seismic attribute analysis of the 2-D sections shows strong attenuation of high frequencies and low similarity of adjacent traces, which correlate with the degree of subsurface erosion induced wave disturbance of the underground.

Key words: sinkhole; subsurface erosion; low velocity zone; shear modulus; Poisson's ratio; seismic attributes.

1 INTRODUCTION

The determination of underground stability and the assignment of zones with an increased probability of sinkhole occurrence in areas affected by subsurface erosion is a challenging scientific question. The subsurface erosion process requires undersaturated water and weak zones within rocks like joints, fractures and faults (Dreybrodt 2004; Johnson 2005). The process creates a variety of large- and small-scale structures such as sinkholes, caves, ground subsidence and springs (Waltham *et al.* 2005). They all represent difficult ground conditions for engineering and construction, and may pose a geohazard in urban areas (Milanovic 2002; Gutiérrez *et al.* 2014). Especially, the sudden formation of sinkholes (Gutiérrez *et al.* 2008; Parise 2019), which can result in building- and infrastructure damage, and life-threatening situations, are a problem all over the world (O'Connor & Murphy 1997; Waltham 2002). This study tests the potential of reflection seismics, especially shear wave reflection seismics and vertical seismic profiles (VSPs) to determine 1-D and 2-D elastic parameters, and seismic attributes for the characterization of sinkhole areas.

1.1 Elastic moduli

Elastic moduli are key parameters that describe stress and strain within the underground, and characterize mechanical properties of rocks (Jaeger *et al.* 2007; Mogi 2007). The rock properties, which depend on, for example lithology, influence the propagation velocity of elastic seismic waves (Mavko *et al.* 2009) and can therefore be used to physically describe the ground stability. They can be described by several parameters, for example, the *P*-wave velocity (V_P), the *S*-wave velocity (V_S), the Young's modulus (E), the shear modulus (μ), the bulk modulus (K) and the Poisson's ratio (ν).

To determine these elastic moduli, geotechnical investigations are necessary (Leroueil 2001). Cone penetration tests and laboratory studies are used in geotechnical engineering for these kinds of investigation, but these methods focus on point or 1-D investigations only, and show lateral variations by interpolation. However, determination of the spatial distribution of elastic moduli of fractured rock masses appears to be advantageous for identification of landslide risk areas (Pazzi *et al.* 2019) or sinkhole risk areas. Besides the direct determination of the elastic moduli by static deformation experiments, measurements of seismic wave velocities can also be used to determine these parameters, because the seismic wave velocity depends on the density and the elastic moduli of a material (Polom *et al.* 2010; Uhlemann *et al.* 2016). When the *P*- and the *S*-wave velocities, and the density of a material are known, the others can be calculated (Table 1). Seismic velocities are common parameters measured in the field and in laboratories, and they are affected by changes of rock- or sediment type, consolidation, crack density, porosity and water saturation (Heap *et al.* 2010; Uhlemann *et al.* 2016). Hence, the generation of cavities and fracture zones due to subsurface erosion (Waltham *et al.* 2005), is expected to influence the elastic moduli, and therefore the wave velocity.

The most important elastic parameter for geotechnical applications is the small-strain shear modulus (μ_0 in Pa), which is used for site characterization, identification of weak zones, seismic hazard-analysis and soil structure interaction (Giannakopoulos & Suresh 1997; Das 2008; Lacroix & Amitrano 2013). μ_0 is calculated from the shear wave velocity in $\mathrm{m\,s^{-1}}$ and the density in $\mathrm{kg\,m^{-3}}$, and describes the material's stiffness, which is defined as the ratio of stress to strain along an axis resulting from shear. Since the shear modulus decreases with increasing shear strain ($\frac{\mu}{\mu_0} \rightarrow$ strain-dependent modulus reduction of the shear modulus μ relative to the small-strain shear modulus μ_0 at zero strain) low values indicate a less stable underground (Mavko *et al.* 2009; Clayton 2011). Static and dynamic values of the described moduli can differ since different measuring methods are used. Static moduli measurements are based on non-elastic deformation of a material by application of a known force, and dynamic moduli are determined by measuring elastic wave velocities (Goodman 1989; Ciccotti & Mulargia 2004). Since seismic wave velocities are used in this study, we always refer to the dynamic shear modulus.

Another commonly used parameter, which describes the stability of slopes (Griffiths & Lane 1999) or the saturation of shallow aquifers (Grelle & Guadagno 2009; Pasquet *et al.* 2015) is the Poisson's ratio (ν). It is calculated using both *P*- and *S*-wave velocities, and in contrast to μ, no density estimation is required, which eliminates uncertainties resulting from density values, for example when taken from literature. The Poisson's ratio of rocks and sediments ranges between 0.2 and 0.5, and describes the ratio of transverse compressional strain to longitudinal extensional strain. For example unconsolidated sediments show a low shear wave velocity due to reduced shear strength, with the result of a high Poisson's ratio (Simm & Bacon 2014).

Both, *P*- and *S*-wave velocities can be determined in the field with cross-hole seismic, down-hole seismic (VSP), reflection- and refraction seismic. A VSP produces a 1-D velocity–depth function, and by a 2-D survey and cross-hole seismic even the lateral, not only the vertical changes, can be determined.

1.2 Seismic attributes

Seismic attribute analysis can further improve the physical characterization of the subsurface. It is used to enhance the seismic interpretation by quantification of characteristics, identification of patterns, and detection of hidden features. According to Barnes (2016), seismic attributes are divided into pre-stack and post-stack attributes, and further subdivided into geological, geophysical and mathematical attributes. Geological attributes describe structural (dip, azimuth, curvature, discontinuity), stratigraphic (reflection spacing, thin-bed thickness) and lithological properties (porosity, density, fluid content), but the latter can only be quantified for pre-stack attributes. Geophysical attributes characterize the seismic wave and the seismic wavelet by quantification of amplitude, phase, frequency and bandwidth. Mathematical attributes describe ratios, variances, averages and other statistical values of seismic data. Over the years many attributes have been developed (Chopra & Marfurt 2007; Barnes 2016). We focus our analysis on post-stack geological/structural and geophysical attributes, in this case continuity, amplitude and frequency.

The instantaneous amplitude, which is independent of phase or polarity, quantifies the magnitude (or reflection strength) of a seismic trace, and shows variations of the seismic reflectivity. To highlight different reflection strengths, we determined the absolute wave energy, which is the sum of all amplitudes squared in a defined time-window of a seismic trace. The frequency describes the number of sinusoidal cycles along a waveform in a given time interval, and is used to quantify seismic wave attenuation. The attribute continuity refers to how consistent the amplitude and phase of a seismic reflection are, whereas the opposite, discontinuity, highlights material cracks induced by faults and/or fractures. It is also called coherence or similarity.

2 STUDY AREAS

The seismic data used for this study were acquired during several field campaigns in 2014–2016, in northern and southern Thuringia in Germany, in and around the towns of Bad Frankenhausen (BF) and Schmalkalden (SK) (Fig. 1). Partly, the subsurface geology of Thuringia is characterized by soluble Upper Permian deposits, for example anhydrite, gypsum and salt. In many areas surrounding the Thuringian Forest and the Thuringian Basin these formations are close to the surface, and sinkholes and subsidence occur due to dissolution and subsurface erosion (Seidel 2003).

BF is located at the southern border of the Kyffhäuser hills, which are a small range of hills in Germany, bounded by the Harz Mountain range to the north and the Thuringian Basin to the south [for an entire regional overview see Seidel (2003)]. The Kyffhäuser hills are bounded by several faults. To the north, is the NW–SE trending Kyffhäuser-Northern-Margin Fault, which belongs both to the Kyffhäuser-Crimmitschau Fault Zone and the Kelbra Fault Zone. The southern part of the hills is bounded by the northward-dipping and W–E striking Kyffhäuser-Southern-Margin-Fault (KSMF, Schriel & Bülow 1926a, b). The sediments in the south of the Kyffhäuser hills are deposits of the Zechstein Sea (258–251 Ma), an epicontinental ocean during the Permian. Due to sealevel changes, conglomerates, carbonates, sulfates and salt were cyclically deposited (Richter & Bernburg 1955). The main marine formations, in order from stratigraphically lower to higher, are Werra, Staßfurt and Leine. The subsurface erosion horizon (S; which consists not only of a small layer, but partly stretches over 70 m of thickness) is located in the Werra- and Staßfurt Formations and consists of soluble anhydrite and gypsum (Richter & Bernburg 1955). The marine sedimentation phase was followed by the terrestrial sedimentation phase of the Triassic. The corresponding

Table 1. Conversion formulas for elastic moduli of homogeneous isotropic linear elastic materials with known *P*- and *S*-wave velocities (Mavko *et al.* 2009). The formulas used in this study are coloured red and symbols are defined in the text.

	V_P	V_S	E	μ	K	ν	Γ
(V_P, V_S)	V_P	V_S	$\frac{\rho V_S^2(3V_P^2-4V_S^2)}{V_P^2-V_S^2}$	ρV_S^2	$\rho(V_P^2-\frac{4}{3}V_S^2)$	$\frac{V_P^2-2V_S^2}{2(V_P^2-V_S^2)}$	$\frac{V_P}{V_S}$

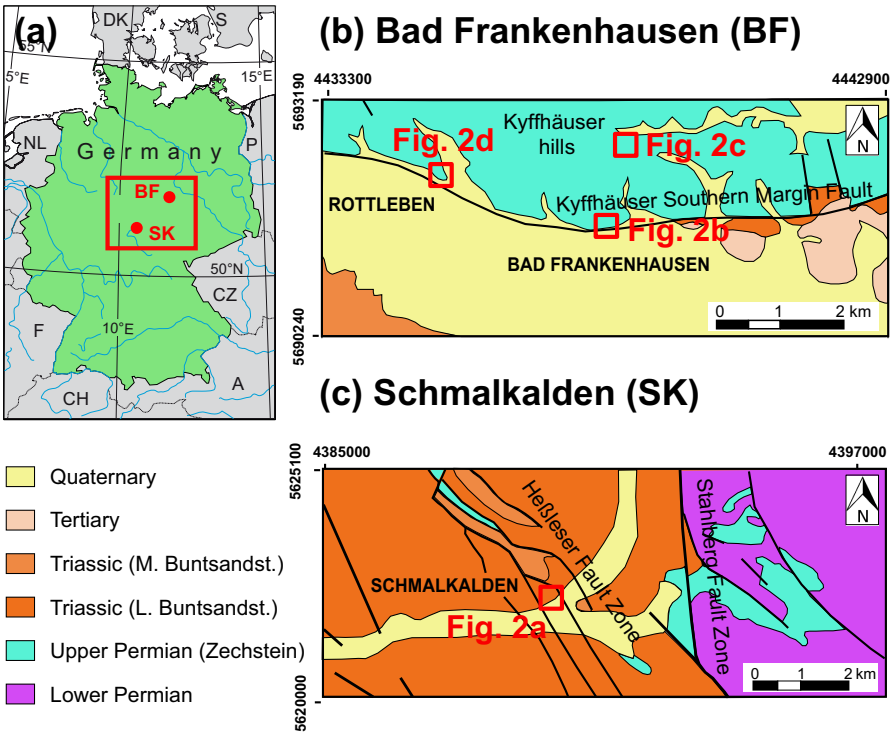

Figure 1. Maps of study areas. (a) Map of Germany showing the location of Thuringia (red square) and Bad Frankenhausen (BF) and Schmalkalden (SK) (red dots), (b and c) geological maps of BF (after Schriel & Bülow 1926a,b) and SK (after Bücking 1906) with location of Figs 2(a)–(d).

deposits of the Middle Buntsandstein (249–244 Ma) are only found at isolated locations, and Cretaceous and Jurassic rocks were completely eroded. During the Early Tertiary, the northern part of the Kyffhäuser hills was uplifted (Freyberg 1923) and tilted, resulting in a 300 m fault throw on the northern margin and a southward-dipping terrain. Therefore, the low hill range is described as a half-horst, as are the Harz Mountains. Tertiary deposits (65–2.6 Ma) are exposed only at a few locations and Quaternary sediments (2.6 –0 Ma), like silt and loess, are widespread (Beutler & Szulc 1999). The entire region south of the Kyffhäuser hills is affected by subsurface erosion as evidenced by salt springs and the occurrence of numerous sinkholes and depressions, which are a result of the combination of soluble rocks (Zechstein Formations) in the near surface and their contact with ground water from the southward-draining hill range that ascends alongside the KSM Fault. They are also an indicator for the long lasting and still ongoing subsurface erosion processes.

SK is located in southern Thuringia. The deeper bedrock below the research area consists of metamorphic gneiss and micaceous shale, which were deformed during the Variscan Orogeny. Later this bedrock was uplifted and formed the Ruhla-Schmalkalden Horst. Like in BF, due to the transgression of the Zechstein Sea during the Permian (258–251 Ma), evaporites were deposited, but due to the horst location, the sediment strata on the Ruhla-Schmalkalden Horst are much thinner than elsewhere in the Thuringian Basin. In SK seven sequences of Zechstein deposits are found, which start with reef dolomite and sulfate rocks of the Werra Formation (Bücking 1906; Dittrich 1966). The following Staßfurt Formation consists of sulfates, claystones and dolomites and the Leine Formation contains claystones and carbonates. The upper part of the Zechstein deposits is represented by claystones, sandstones and dolomites of the Leine, Aller, Ohre and Friesland formations, and finishes with sand- and claystones of the Fulda Formation (Schmidt *et al.* 2013). The Zechstein Formation is followed by terrestrial sediments of the Triassic, for example the Calvörde and Bernburg formations of the Lower Buntsandstein (251–249 Ma), and because of intense erosion due to fault movement, mostly since the Upper Cretaceous, which also led to the uplift of the Thuringian Forest, these formations are also the youngest beds to outcrop in the region, except for a thin layer of Quaternary deposits (2.6–0 Ma). The Heßleser Fault Zone crosscuts the town of SK, and therefore the study area, and contains several smaller fault branches. In November 2010 a large sinkhole opened up in the residential area. The sinkhole was 26–30 m in diameter, 12–17 m in depth and the crater had a volume of 4000–4200 m^3 (Schmidt *et al.* 2013). The bedrock, which was visible within the crater, was strongly fractured and showed small-scale faults and folding of layers. The damage caused by the collapse, such as cracks in houses and streets, was mainly concentrated on the areas north and northeast of the sinkhole. Although this is the first known sinkhole in the urban area of SK, several salt water springs can be found in the surrounding area, which also indicate

the long-lasting dissolution processes in this region (Schmidt *et al.* 2013).

3 METHODS

3.1 Seismic data acquisition and processing

Reflection seismic surface data (S_H wave) and borehole data (P, S_H and S_V wave) were acquired during several field campaigns (Fig. 2). As seismic source for the 2-D reflection seismic profiles an electrodynamic microvibrator (ELVIS S) was used. For borehole SK 05-2011 the mini-vibrators MHV P and MHV S were used as seismic sources, and for the other three boreholes (BF 01-2014, BF 02-2014 and BF 01-2012) the microvibrators ELVIS P and ELVIS S were used, due to unavailability of one of the mini-vibrators. Since the ELVIS source has a lower force and the underground showed strong attenuation of seismic waves, the investigation depth is lower, but the subsurface erosion horizon was still reached. As receivers horizontal geophones attached to a landstreamer and a three-component (3C) geophone in a borehole probe were utilized. For an overview of the 2-D reflection seismic survey parameters see Table 2, and for the corresponding data processing see Table 3 and Wadas *et al.* (2016, 2017, 2018). For all 2-D profiles a manual and interactive stacking velocity analysis was carried out based on semblance, offset gathers and constant velocity stacks. The interval velocity fields derived from stacking velocities are the data base for calculation of 2-D elastic moduli, and the post-stack migrated time sections were used for seismic attribute analysis.

For the VSP surveys, the seismic sources had a fixed position of 1–3 m distance to the borehole (near-offset VSP), and the borehole probe with a 3C-geophone was continuously pulled up in 2 m intervals. At each receiver position, two sweeps of each source (P and S) were excited for improvement of signal-to-noise ratio (S/N ratio). The dense receiver spacing was required to detect small seismic velocity changes with depth. The first steps of VSP data processing consisted of vibroseis correlation, geometry installation, vertical stacking, and amplitude scaling of multiple records, as for 2-D data processing. Afterwards the recorded channels for the P wave and the S wave were split into the X, Y and Z components. The amplitudes of the first arrivals were enhanced by application of an automatic gain control and trace normalization, and the S/N ratio was improved by application of bandpass-, notch- and/or frequency-wavenumber filters. Finally, the first arrivals were manually picked to achieve a velocity function with depth.

3.2 Determination of elastic moduli

For calculation of μ in 1-D and 2-D, the formula of Table 1 was used with density values based from literature (Table 4) and seismic interval velocities derived from reflection seismic field data. Since the velocity is squared for the calculation of μ, the influence of the density is less pronounced, so the use of density values taken from literature is acceptable, if *in situ* rock densities are not available. The Poisson's ratio is calculated using the formula of Table 1 with the P- and S-wave interval velocities, and it was determined for all boreholes in 1-D. For the analysis of elastic moduli, the processing software VISTA Version 10.028 by Gedco (now Schlumberger) was used.

For a better assessment of the seismic results, apparent electrical resistivity and gamma ray measured in the boreholes are suitable methods. The gamma ray borehole probe detects the natural radiation from the different formations in counts per second. Therefore, it is suited to detect changes in lithology, for example evaporites show a low radiation level and shales show a high radiation level (Liu 2017). For that reason it is used to verify the trend of density–depth curves, since density can depict lithology changes too. The resistivity/conductivity was determined using an array induction probe (40 kHz) which consists of a transmitter coil and four receiver coils. The alternating current at the transmitter coil generates a primary magnetic field. The primary magnetic field causes eddy currents in the formation that are proportional to the formation conductivity. These eddy currents generate a secondary magnetic field which induces an alternating current in the receivers coils. The detected resistivity/conductivity is used to identify water-saturated zones (Liu 2017), which might help to detect zones affected by dissolution of soluble rocks.

3.3 Determination of seismic attributes

The seismic attributes were determined for the migrated time-sections of four 2-D shear wave reflection seismic profiles using the software OpendTect by dGB Earth Sciences with a focus on frequency and similarity. The attribute analysis tool of OpendTect was used to return the arithmetic mean of the frequency spectrum of a migrated time-section called average frequency (dGB Beheer 2017). In order to compare results, the frequencies were normalized. The multitrace attribute 'similarity', a kind of cross-correlation, compares two or more trace segments and describes how much the trace segments look alike. The trace segments are defined by a time-gate in ms and the positions are specified by a trace step-out. Here four traces were compared. The values range from 0 to 1, a similarity of 0 means the traces are completely dissimilar with respect to waveform and amplitude, and a similarity of 1 states that the traces are identical.

4 RESULTS

4.1 Elastic moduli, gamma ray and electrical resistivity of boreholes

In four boreholes at two different locations (BF and SK, Figs 1 and 2) V_P, V_S, μ and ν were determined. Besides the density values (Table 4) used for its calculation, gamma ray logs for each borehole and electrical resistivity measurements of boreholes 02-2014 and 01-2012 are shown. All the velocity- and moduli-depth curves start at 2 m below surface and they reach different depths, respectively.

In borehole SK 05-2011 (Fig. 3), between 2 and 80 m depth, the seismic waves and their corresponding velocities show typical values for compacted rocks/sediments ((Brückl *et al.* 2005) and references therein). The velocities are generally increasing with depth and mostly the P wave is at least twice as fast as the S wave for sandstone, claystone, gravel and/or silt. But when the seismic waves reach the subsurface erosion horizon that consists of anhydrite and gypsum, they change their behaviour. Between 80 and 130 m depth the S-wave velocity (V_S) increases from 1500 to 3000 m s^{-1} and then decreases to *ca.* 1600 m s^{-1}, and the P-wave velocity (V_P) increases from 2000 to 4000 m s^{-1} and then decreases to 2000 m s^{-1}. So, the velocities of V_P and V_S for this zone seem to be almost the same, which contradicts the wave theory.

The similarity of V_P and V_S is not a result of poorly visible and wrongly picked first breaks as shown by, for example the VSP data

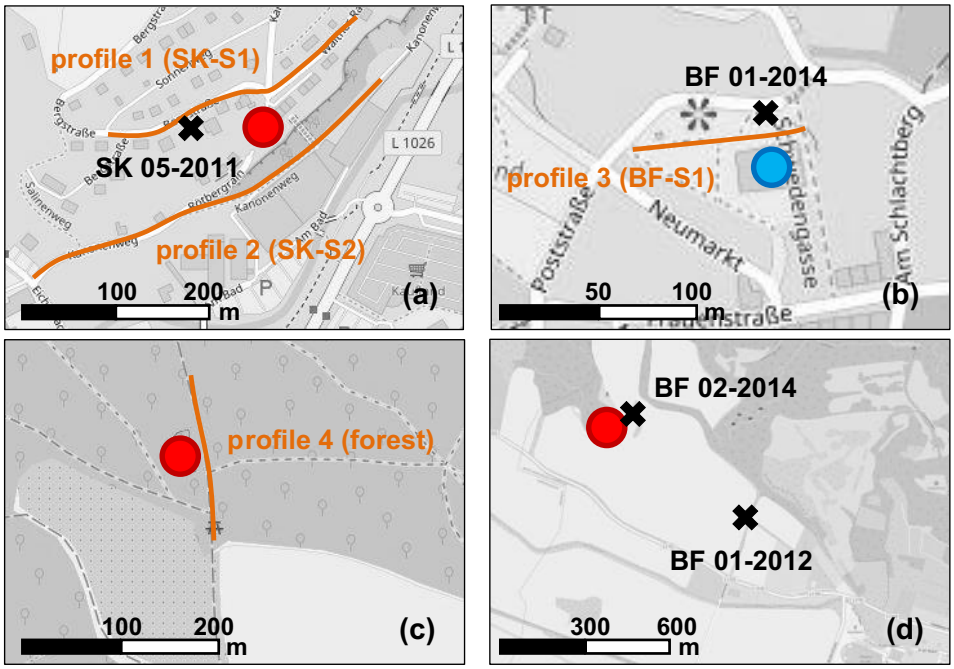

Figure 2. Location maps of the S_H-wave reflection seismic surveys and the VSPs. (a) shows the location of borehole SK 05-2011 and profiles 1 and 2 (see also (Wadas *et al.* 2017)), (b) illustrates the location of borehole BF 01-2014 and profile 3 (see also Wadas *et al.* 2016), (c) displays the position of profile 4 (see also Wadas *et al.* 2018) and (d) features the position of boreholes BF 02-2014 and BF 01-2012. Red dots mark positions of sinkholes and the blue point marks the position of the subsurface erosion induced leaning church tower of BF.

Table 2. Acquisition parameters of the 2-D S_H-wave reflection seismic profiles and the VSPs.

	S_H-wave reflection seismic	VSP
Source type	MHV S and ELVIS S	MHV P/S and ELVIS P/S
Source signal	20–120 Hz (10 s)	20–120 Hz (10 s)
Source spacing	2/4 m	*ca*. 1–3 m from borehole (fixed)
Number of sweeps per source point	4 sweeps	2 sweeps
Receiver type	1C-geophone (horizontal)	3C-geophone
Receiver spacing	1.0 m	2.0 m
Recording system	Geometrics Geode	Geometrics Geode
Record length	12 s uncorrelated	12 s uncorrelated
Sampling interval	1 ms	1 ms

Table 3. Overview of processing steps applied to the 2-D reflection seismic profiles.

Profiles 1 and 2 (SK-S1 and SK-S2)	Profile 3 (BF-S1)	Profile 4 (BF-forest)
Correlation	Correlation	Correlation
Geometry	Geometry	Geometry
Amplitude and spectral editing	Amplitude and spectral editing	Amplitude and spectral editing
Vertical stack	Vertical stack	Vertical stack
Top mute	Top mute	Top mute
Spectral balancing	Freq. Filter	Freq. Filter
Freq. Filter	Data sorting	Offset-dependent, time-variant log. scaling
Data sorting		Data sorting
Velocity analysis	Velocity analysis	Velocity analysis
NMO and static correction	NMO and static correction	NMO and static correction
CMP stack	CMP stack	CMP stack
Freq. Filter	Freq. Filter	Freq. Filter
	Spectrum balancing	Spectrum balancing
		Coherency enhancement
FD time migration	FD time migration	FD time migration
Depth conversion	Depth conversion	Depth conversion

Table 4. Literature values (Brückl *et al.* 2005) used for density–depth curves.

Rock type	Density [g cm^{-3}]	Rock type	Density [g cm^{-3}]
Dry sand	2.33–2.80	Sandstone	2.30–2.55
Wet sand	1.50–2.00	Dolomite/carbonate	1.75–2.88
Gravel	1.95–2.20	Gypsum	2.31–2.33
Clay	1.25–2.32	Anhydrite	2.15–2.44
Claystone	2.65–2.75		

of borehole SK 05-2011 (Fig. 4). The first breaks are clearly visible due to their high amplitudes, but between 80 and 130 m depth the first breaks of the *S* wave show nearly the same gradient as the first breaks of the *P* wave. So the velocities of both wave types are almost the same for this zone, which is physically unreliable (Lowrie 2007). This similarity in wave speed is observed for different boreholes in different study areas and correlates with the subsurface erosion horizons. In the discussion section, we take a closer look at this phenomenon.

For borehole SK 05-2011, the Poisson's ratio is shown between 2 and 80 m depth only (Fig. 3), because between 80 and 140 m depth the almost similar velocities of *P* and *S* wave would result in a negative ratio. Materials of negative Poisson's ratio do exist and they are called auxetic materials. When these materials are stretched in one axis they become thicker perpendicular to the applied force, for example specific polymers such as GoreTex (Fahlman 2011). For this reason Poisson's ratios beyond the range of 0.2–0.5, which are a result of too high shear wave velocities, are not shown. Between 2 and 80 m depth the Poisson's ratio ranges from 0.48 to 0.10. The low V_S for the claystones and sandstones between *ca*. 30 and 60 m result in a high Poisson's ratio with values between 0.40 and 0.48 that indicate a reduced stability of the material. Within the carbonate and dolomite rocks below, the ratio decreases from 0.40 to 0.17, which means the material is more resistive against deformation. The shear modulus was calculated for 2–74 m depth only, due to unrealistic V_S values for greater depths. Usually, μ increases with depth from 100 to 3200 MPa, which indicates a high shear strength, but several zones with reduced values are observed above the subsurface erosion horizon. Such zones are between 25 and 35 m depth in the sandstone formation with 530 to 860 MPa, and between 62 and 68 m depth in the carbonate formation with 1600 MPa. For the carbonate rocks the core inspection revealed a disrupted and fractured zone.

Borehole BF 01-2014 (Fig. 5) shows the same characteristics as borehole SK 05-2011. The first 2–6 m consist of anthropogenic and Quaternary deposits, and V_P ranges between 646 and 547 m s^{-1} and V_S ranges between 406 and 270 m s^{-1}. The subsurface erosion horizon is located between 6 and 73 m depth, and between 20 and 67 m depth the core material indicates several small cavities. In the subsurface erosion horizon the apparent V_S is as fast as V_P (*ca*. 1200 m s^{-1} at 30 m depth) similar to the observations made for borehole SK 05-2011, or it even exceeds V_P (700–1200 m s^{-1} for the *P* wave and 530–1800 m s^{-1} for the *S* wave between 40 and 67 m depth). Regarding the Poisson's ratio, the values vary from 0.09 to 0.41 between 2 and 22 m depth and the zone between 22 and 70 m depth shows unrealistic values beyond the range of 0.2–0.5, due to a too high V_S and a too low V_P. The carbonate that marks the top of the subsurface erosion horizon shows a Poisson' ratio of 0.46–0.48 indicating a lower ground stability. The anhydrite and gypsum below the carbonate have relatively low values of 0.19–0.31, which indicates a more stable formation that is not affected by subsurface erosion. The shear modulus μ for borehole BF 01-2014 (Fig. 5) increases between 2 and 32 m depth from 140 to 3800 MPa and decreases between 32 and 50 m depth from 3800 to 150 MPa. From 50 to 67 m depth the shear modulus was not calculated, due to the unrealistic V_S values as described above. Below the subsurface erosion horizon from 74 to 90 m depth μ shows varying values, but an increase from 240 to 2900 MPa is observed.

Borehole BF 02-2014 (Fig. 6) shows mostly realistic V_S values, except for small areas between 46 and 50 m depth, and between 80 and 84 m depth, where V_S reaches almost V_P. From 2 to 45 m depth, *P*- and *S*-wave velocity increase with depth (480–2430 m s^{-1} for V_P and 142–1000 m s^{-1} for V_S), but between 54 and 78 m depth V_P increases from 1840 to 4750 m s^{-1}, while V_S still has low values of 1100–1900 m s^{-1}. This results to a high Poisson's ratio of 0.38–0.47, which indicates a less stable zone. μ shows an increase between 2 and 74 m depth from 50 to 8000 MPa, although a zone within the subsurface erosion horizon with lower values of *ca*. 2500–5000 MPa is observed from 50 to 68 m depth. The anhydrite and gypsum of this zone show several small cavities and the electrical resistivity logs display a reduced apparent resistivity of 12–80 Ωm. Both μ and the resistivity indicate dissolution-induced cavity formation, and therefore reduced ground stability. Between 74 and 88 m depth a high μ peak is observed with up 14 500 MPa that results from too high V_S values and this phenomenon correlates with the subsurface erosion horizon. The electrical resistivity log shows three other zones with reduced values of less than 10 Ωm between *ca*. 70 and 96 m depth. At the end of borehole BF 02-2014, between 88 and 104 m depth, μ varies from 4900 to 6800 MPa.

Borehole BF 01-2012 (Fig. 7) shows almost constantly increasing velocities between 2 and 24 m depth, with 300–1100 m s^{-1} for V_P and 200–300 m s^{-1} for V_S. In the subsurface erosion horizon between 26 and 46 m depth, V_S seems to equalize with V_P, as it is observed for the other boreholes. From 47 to 66 m depth V_P increases again up to 2600 m s^{-1} and V_S remains low at only 690 m s^{-1}. This results to a high Poisson's ratio of 0.40–0.47, which indicates an unstable area and the analysis of cores revealed several small cavities in this zone. μ increases with depth, but shows much smaller values as for the other boreholes. Except for two peaks at *ca*. 28 m depth and between 60 and 66 m depth, μ ranges between 80 and 850 MPa. Within the subsurface erosion horizon between 30 and 50 m depth values from 80 to 340 MPa are observed that indicate a reduced shear strength, and therefore a less stable underground. The area between 30 and 66 m depth also correlates with a zone of very low resistivity values of less than 10 Ωm, which further indicates a less stable zone due to dissolution of soluble rocks.

4.2 Shear wave velocity and shear modulus of 2-D profiles

The shear modulus was also determined in 2-D across four shear wave reflection seismic profiles (Figs 2 and 8). Profile 1 was surveyed north of the urban sinkhole in SK (Fig. 2a) and shows a large subsurface erosion induced depression between 0 and 170 m profile length from 10 to 40 m depth (Wadas *et al.* 2017). The shear wave velocity across the profile ranges from 210 to 545 m s^{-1} with a low velocity zone between *ca*. 40 and 70 m depth that consists of values from 210 to 300 m s^{-1} (Fig. 8.1a). According to the core inspection, this zone, which is located above the subsurface erosion horizon, correlates with disrupted and fractured sandstones and claystones. It also shows low μ values of 100–250 MPa, which indicate less ground stability due to reduced shear strength. In general μ ranges between *ca*. 100 and 700 MPa and high μ values are identified for the subsurface erosion horizon, which is located between *ca*. 80 and 140 m depth (Fig. 8.1c). The μ-values are the result of high V_S

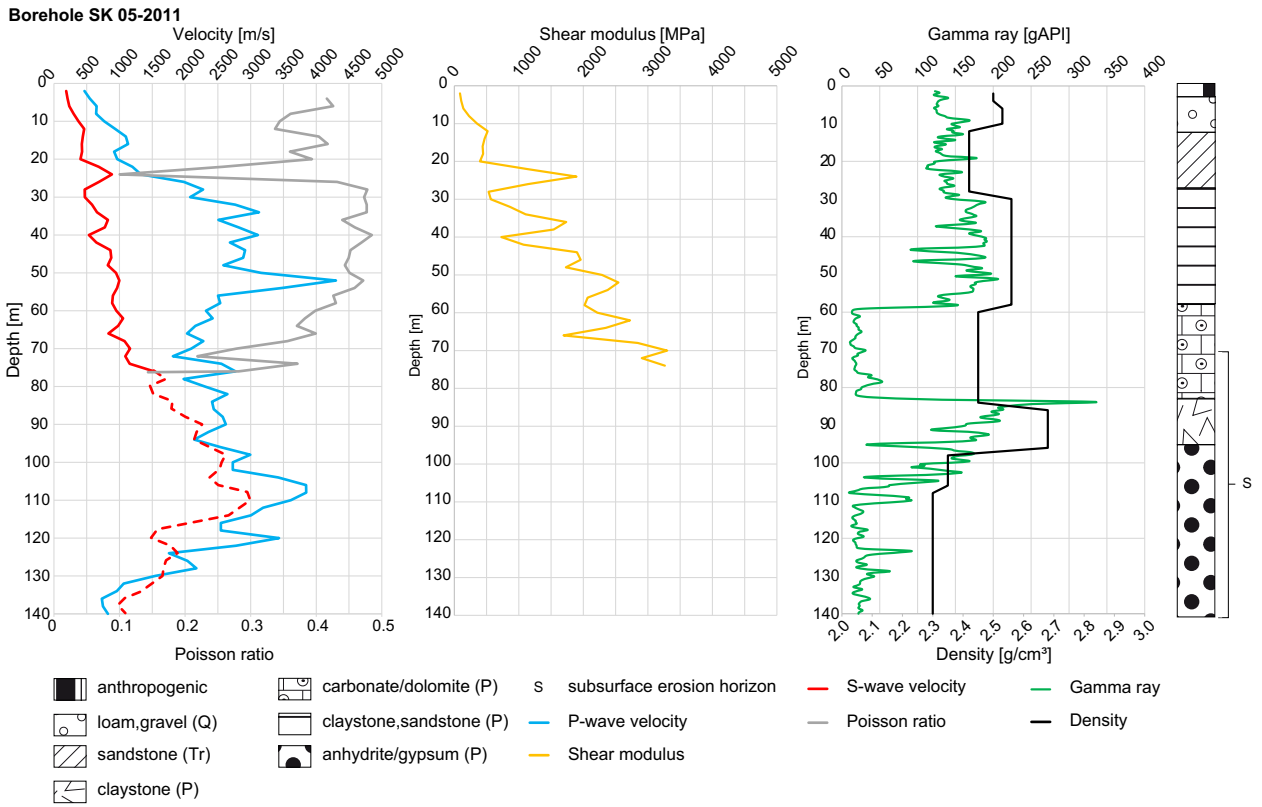

Figure 3. Velocity/moduli-depth curve of borehole SK 05-2011 with stratigraphy showing P-wave-(blue) and S-wave velocities (red), Poisson's ratio (grey), shear modulus (orange), density (black), gamma ray (green), and stratigraphy.

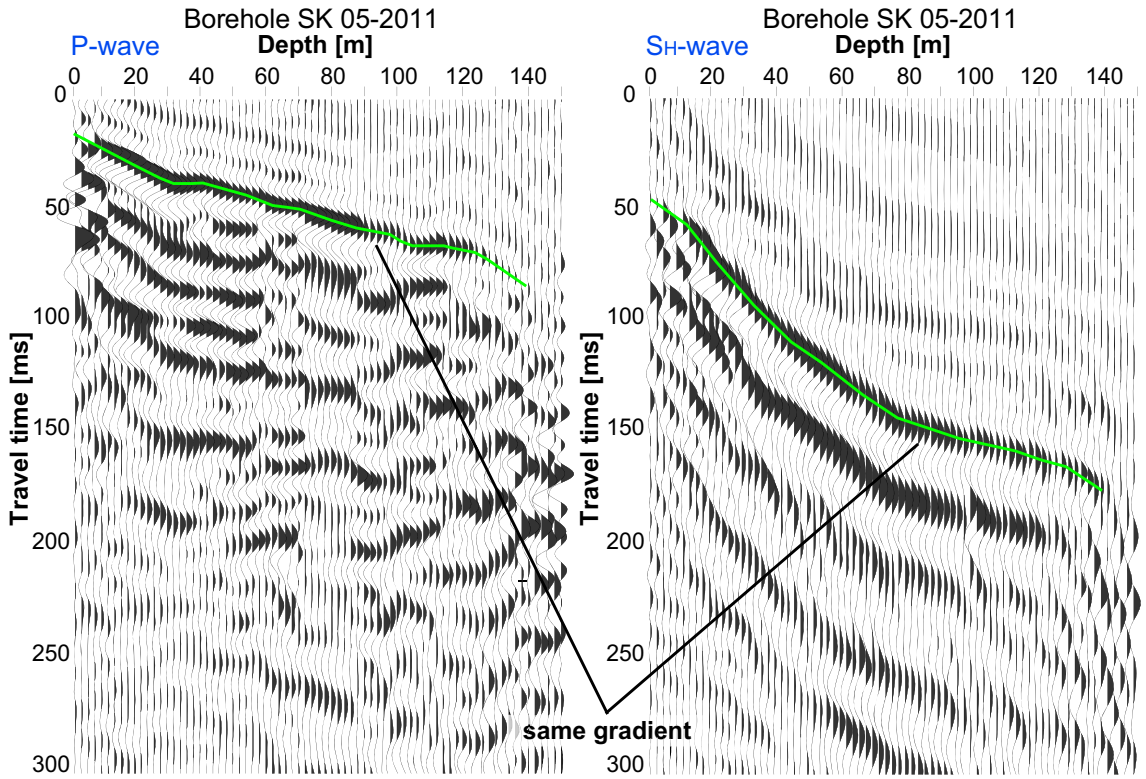

Figure 4. VSP data of borehole SK 05-2011 with picking line of first breaks (green). Between 80 and 130 m depth, the *S* wave (Y-component; right) shows the same gradient, and therefore similar velocities as the *P* wave (Z-component; left). This indicates a wave conversion from *S*-to-*P* wave in the depth of the subsurface erosion horizon. The map on the left shows the location of the borehole (see also Fig. 2).

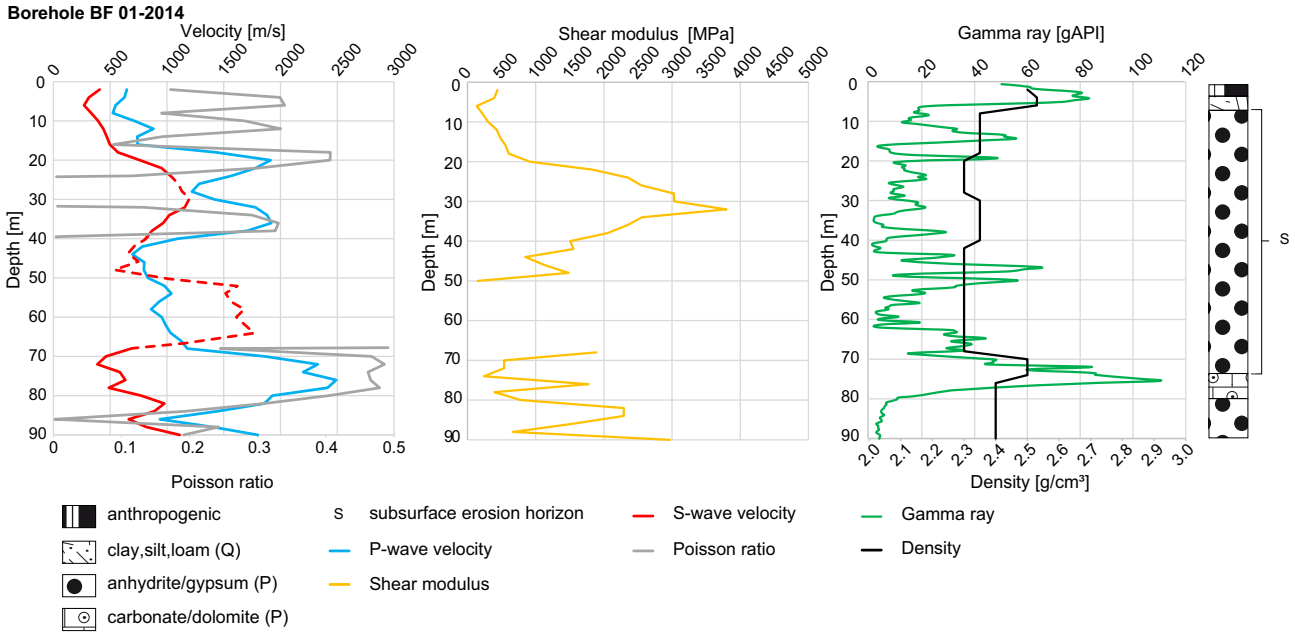

Figure 5. Velocity/moduli-depth curve of borehole BF 01-2014 with stratigraphy showing *P*-wave (blue) and *S*-wave velocities (red), Poisson's ratio (grey), shear modulus (orange), density (black), gamma ray (green) and stratigraphy.

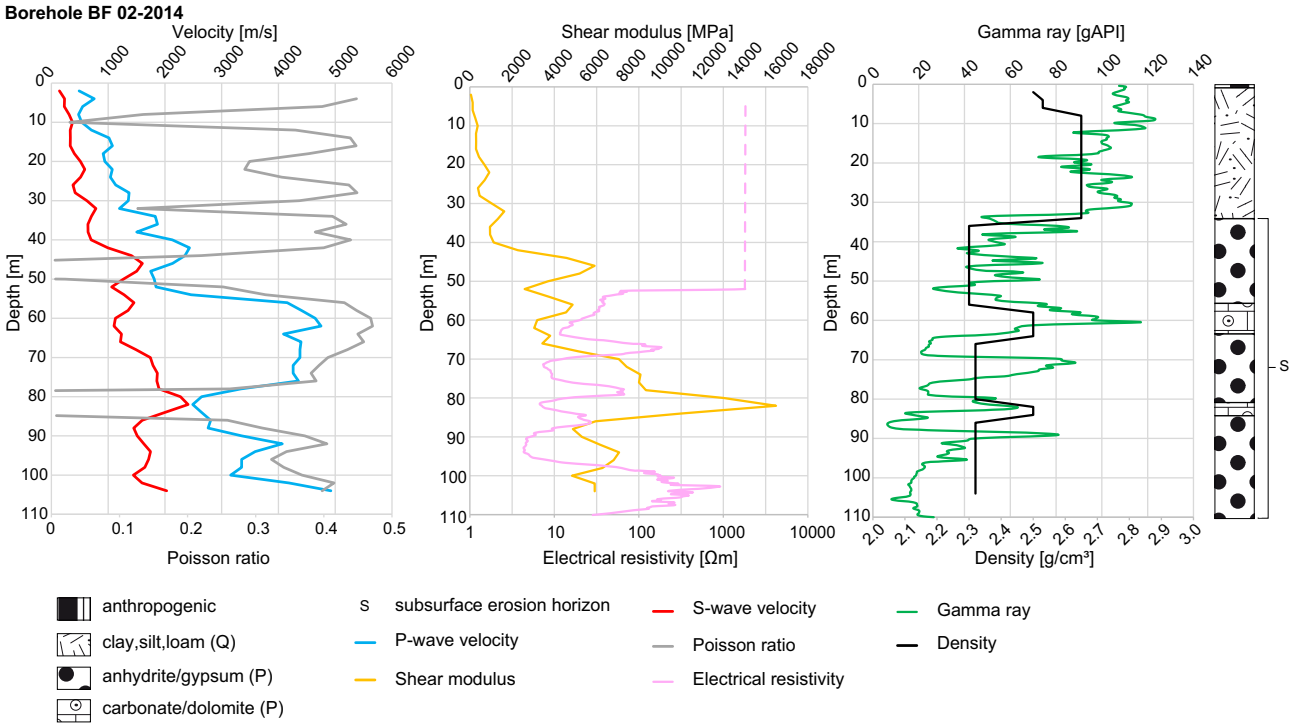

Figure 6. Velocity/moduli-depth curve of borehole BF 02-2014 with stratigraphy showing P-wave-(blue) and S-wave velocities (red), Poisson's ratio (grey), shear modulus (orange), density (black), gamma ray (green), resistivity (pink), and stratigraphy.

values and this coincides with the observations from borehole SK 05-2011 and is also observed for profile 2.

Profile 2 was surveyed south of the urban sinkhole in SK (Fig. 2a) and shows two depressions between 0 and 170 m profile length and between 250 and 330 m profile length from 0 to 30 m depth (Wadas *et al.* 2017). V_S generally increases with depth, but the near-surface down to 60 m depth is characterized by low velocities from 198 to 350 m s^{-1} (Fig. 8.2a). The corresponding μ values range between *ca.* 75 and 250 MPa and indicate unstable strata. This correlates with the observations from borehole SK 05-2011. In total μ ranges between 75 and >800 MPa (Fig. 8.2c).

Profile 3 was surveyed in the town of BF, north of a subsurface erosion induced leaning church tower (Fig. 2b), which is located between *ca.* 60 and 80 m profile length (Wadas *et al.* 2016). Generally V_S ranges between *ca.* 120 and 475 m s^{-1}, and between 40 and 86 m profile length from 0 to 40 m depth a low velocity zone

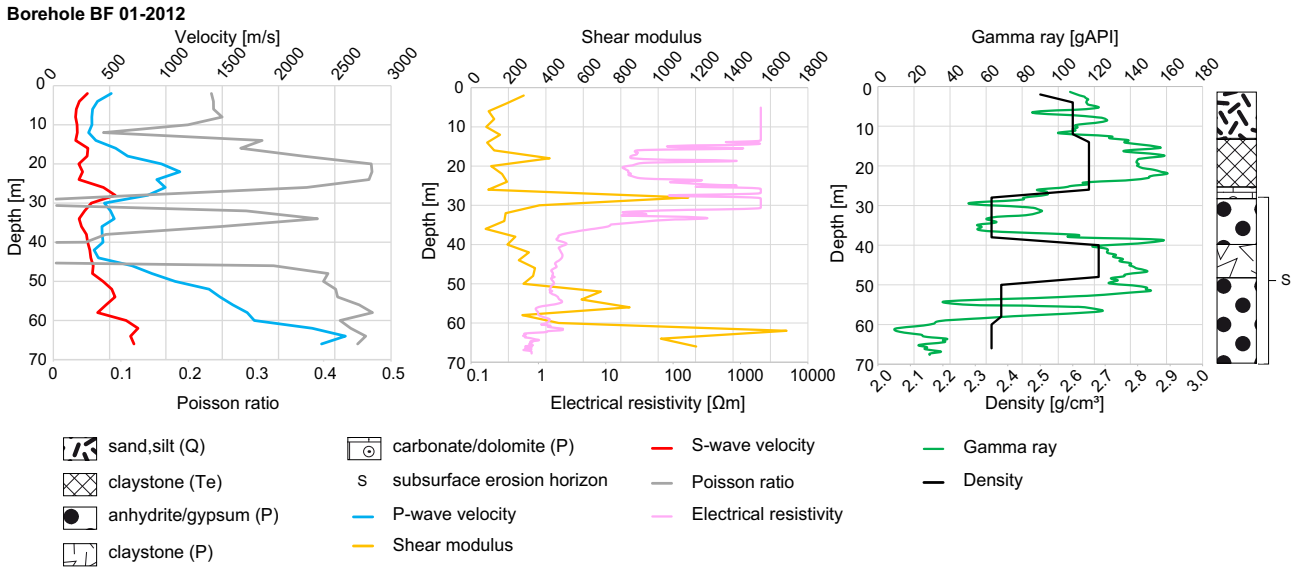

Figure 7. Velocity/moduli-depth curve of borehole BF 01-2012 with stratigraphy showing *P*-wave (blue) and *S*-wave velocities (red), Poisson's ratio (grey), shear modulus (orange), density (black), gamma ray (green), resistivity (pink) and stratigraphy.

is observed with V_S values of 120–250 m s^{-1} (Fig. 8.3a). μ shows severely reduced values below the tower of around 25–100 MP. Such low shear strength indicates a highly unstable underground and the core analysis of BF 01-2014 revealed several small cavities in this depth. Overall μ ranges from 25 to 525 MPa for this profile (Fig. 8.3c).

Profile 4 was surveyed north of the town BF, parallel to a sinkhole in a forest (Fig. 2c). The soluble rocks, and therefore the subsurface erosion horizon, are found a few metres below the surface down to 60 m depth. The sinkhole is visible between 50 and 130 m profile length and several collapse events are imaged within the subsurface erosion horizon, which indicate different stages of sinkhole development (Wadas *et al.* 2018). V_S shows values between *ca*. 150 and 500 m s^{-1} and the lowest values are between 0 and 60 m depth with 150–325 m s^{-1} (Fig. 8.4a). The corresponding shear modulus ranges between *ca*. 50 and 725 MPa, but the soluble rocks show values of only 50–250 MPa, indicating a low shear strength (Fig. 8.4c).

4.3 Seismic attributes frequency and similarity

For the four shear wave reflection seismic profiles presented in Fig. 8, a seismic attribute analysis was carried out using the migrated time sections. The average and normalized frequencies (*X*-axis) and similarities (*Y*-axis) are shown as cross-plots with colour-coded energy values (Fig. 9). A similarity of 1 indicates that the compared traces are identical and a similarity of 0 indicates that the traces are different. For example, undisturbed and horizontally layered deposits would have a relatively high similarity near 1, but fractured formations with displaced layers would result in a relatively low similarity, for example smaller than 0.3. Similar statements can be made for the frequency, because disrupted formations with small-scale structures lead to enhanced scattering and attenuation, which results in a loss of higher frequencies (Chopra & Marfurt 2007). The 'energy', an amplitude-based attribute without unit, shows low energy near 0 in blue and high energy up to 10 in red. A high impedance contrast, as a result of high density and/or velocity contrasts between two formations, will lead to high energy values (Chopra & Marfurt 2007; dGB Beheer 2017). A fractured and disrupted subsurface smears the density contrasts, resulting in low energy values.

Profile 1 and profile 2 (Fig. 2a) were acquired north and south of an urban sinkhole in the town of SK using a source signal of 20–120 Hz. The recorded useful signal has a frequency range of only 20–80 Hz (Figs 9a and b), which indicates attenuation of higher frequencies (to remove noise above 80 Hz filters were applied). The attribute analysis further revealed that profile 1, located north of the sinkhole, shows more dissimilarities regarding waveform and amplitude, compared to profile 2 located south of the sinkhole. For profile 1 the similarity ranges between 0.9 and 0.1 (Fig. 9a), and for profile 2 the similarity ranges between 0.9 and 0.3 (Fig. 9b). For both profiles, the highest energy is focused on the lower frequencies between 20 and *ca*. 40 Hz at high similarity values. The strong attenuation of high frequencies and the low similarity values correlate with the degree of subsurface erosion induced disturbance of the underground. A detailed structural *S*-wave seismic analysis of the area surrounding the sinkhole revealed that the underground north of the sinkhole is more disturbed than to the south (Wadas *et al.* 2017).

Profile 3 (Fig. 2b) used a sweep frequency range from 20 to 120 Hz and the recorded data shows useful signal response of 25–80 Hz, which is similar to the observations made for profile 1 and profile 2. In contrast, the similarity reveals more dissimilarities with values between 0.8 and 0.0 (Fig. 9c), and the energy shows significantly lower values, especially for lower frequencies, compared to profile 1 and profile 2. The differences between profile 1 and 2 and profile 3 display the differing ground conditions of the two study areas of SK and BF. Profile 3 was acquired north of the subsurface erosion induced leaning church tower of BF and the underground below the tower is more fractured than the subsurface below SK. This might be because the subsurface erosion processes are more intense in BF, and anhydrite and gypsum are much shallower (Wadas *et al.* 2016) compared to SK (Wadas *et al.* 2017). Additionally, in BF brine production is still ongoing, which probably enhances the natural processes and the resulting subsurfaces disturbances.

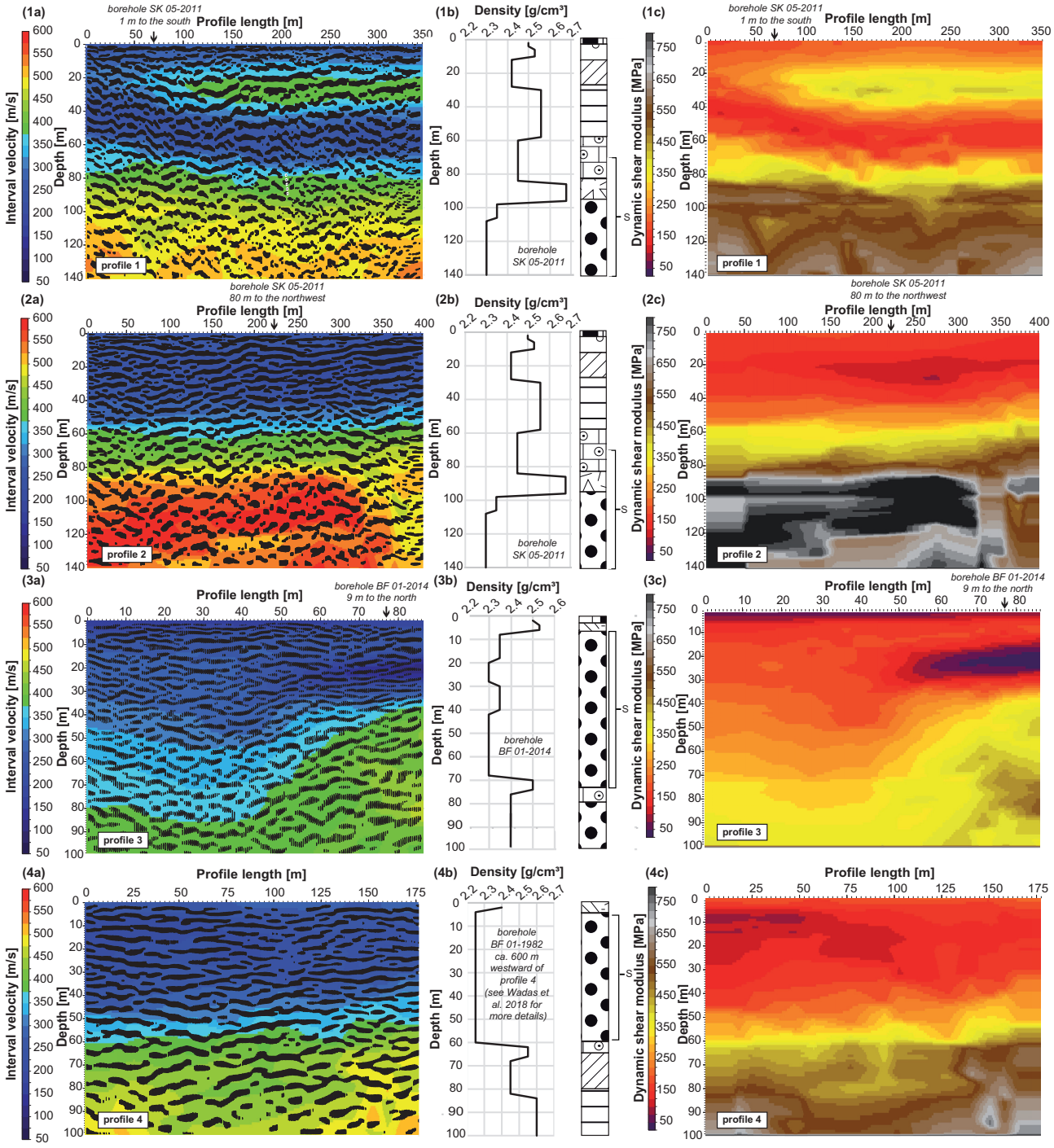

Figure 8. Shear modulus of 2-D reflection seismic. Shear wave velocity (a), density and stratigraphy (b), and shear modulus (c) of four 2-D reflection seismic profiles surveyed in areas affected by near-surface dissolution of soluble rocks (Fig. 2). Profile 1 and profile 2 were surveyed in SK north and south of a sinkhole (Wadas *et al.* 2017), profile 3 was surveyed north of the subsurface erosion induced leaning church tower of BF (Wadas *et al.* 2016), and profile 4 was carried out parallel to a sinkhole north of BF (Wadas *et al.* 2018). The lithology pattern is described in Fig. 3.

Profile 4 (Fig. 2c), surveyed parallel to a sinkhole, shows a frequency range of *ca*. 25–80 Hz similar to profiles 1–3, and the similarity values range between 0.9 and 0.0 (Fig. 9d) similar to profile 3. For this profile, the energy attribute seems to depend on frequency only, because high energy is not focused on high similarity values as observed for profiles 1–3. The comparability of profile 3 and 4 is given, because profile 4 was also acquired in BF, and shows comparable ground conditions with soluble Permian deposits close to the surface.

In general, the seismic attribute analysis revealed strong attenuation of frequencies >80 Hz and low similarity of adjacent traces, which correlate with the degree of subsurface erosion induced disturbance of the underground. Both are a result of the presence of fractures and intraformational faults due to mass-movement in-

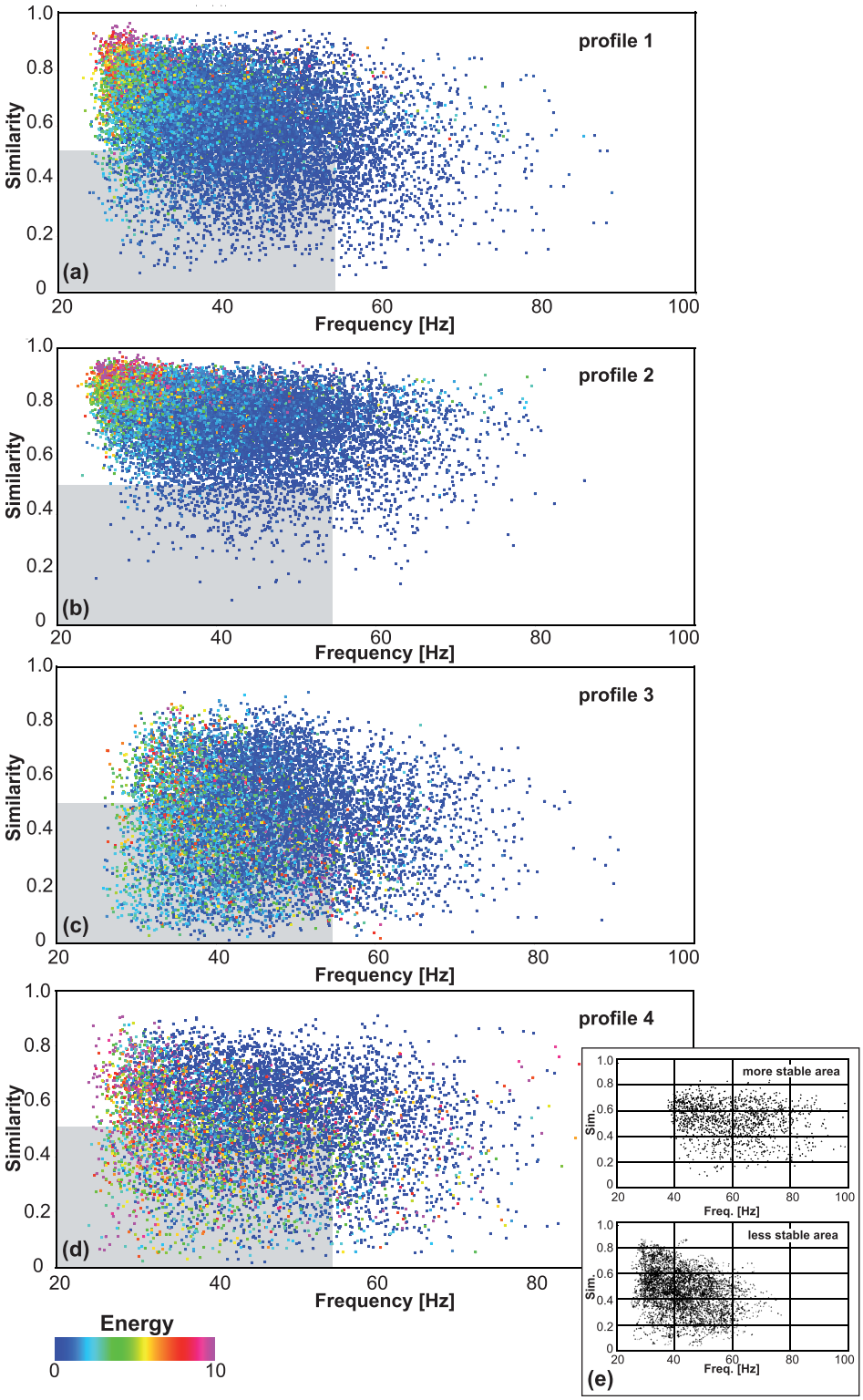

Figure 9. Cross-plots showing the seismic attributes similarity, frequency and energy of the four S_H-wave reflection seismic profiles (a–d). Based on the results of this study low frequencies between 20 and 55 Hz in combination with low similarities between 0.0 and 0.5 indicate highly unstable areas (marked by grey box). (e) As an example, for profile 4 the differences between more stable and less stable areas are shown.

duced by subsurface erosion. As an example, Fig. 9(e) shows the difference in frequency and similarity between more stable and less stable areas for profile 4. More stable areas in profile 4 are characterized by frequencies from 40 to 80 Hz and a similarity between 0.4 and 0.8, whereas less stable areas show frequencies from 25 to 60 Hz and similarities between 0.0 and 0.6. Taking the results of all profiles into account, similarity and frequency are especially suited to detect and quantify lateral changes and heterogeneities in

the subsurface and can be used to define critical parameters regarding ground stability. Based on the results of this study, we suggest that low frequencies between 20 and 55 Hz, in combination with low similarities between 0.0 and 0.5, indicate highly unstable areas (marked by grey box in Fig. 9).

5 DISCUSSION

5.1 Low velocities indicate fractured zones

Geotechnical parameters, such as μ or ν, are mandatory for a successful modelling of sinkhole formation and subsurface erosion processes (Al-Halbouni *et al.* 2018, 2019), and in this study they were calculated from seismic wave velocities. Except for zones which indicate a wave conversion from *S*-to-*P* wave (see Section 5.2, for details), V_S of the presented data shows mostly low to very low values ranging from 142 to 1900 m s^{-1} in VSP surveys and 120 to 545 m s^{-1} for the 2-D surface profiles. The slowest V_S values range from 120 to 350 m s^{-1} for the 2-D surface profiles and from 200 to 400 m s^{-1} for the VSP surveys and are found in low velocity zones within or above the subsurface erosion horizon. V_P was only determined by VSPs and shows values between 300 and 4750 m s^{-1}. Compared with surface seismics, the VSPs show higher seismic wave velocities, which is assumed to be a result of the wave propagating only once through the fractured low-velocity zone and the inaccuracy of the stacking velocity analysis in 2-D compared to a direct wave speed measurement in VSPs.

We propose that the low-velocity zones are a result of the subsurface erosion processes and the associated generation of fractures, cavities and collapse structures (Krawczyk *et al.* 2012). Mass-movement induced by dissolution of soluble rocks generates small cavities that are growing larger over time due to continuous rock failure (Gutiérrez 2010; Parise 2010). According to Kowalski (1991), Schneider-Löbens *et al.* (2015) and Al-Halbouni *et al.* (2018), rock failure is influenced by stress distribution in intact rocks, bedding and fractures. Cavities are unable to transfer stress, and therefore the stress distribution in the surrounding material changes. Formation failure starts in the central upper part of the cavity with fracture initiation. Pre-existing and new fractures form a complex fracture network and reduce ground stability significantly, especially in the area above the cavity. Due to increasing rock failures the cavity becomes larger and this is accompanied by further fracture formation (Kowalski 1991; Schneider-Löbens *et al.* 2015; Al-Halbouni *et al.* 2018). Depending on the fracture network, the size and shape of the cavity itself and the thickness of the overburden, either a sinkhole or a depression can form (Waltham *et al.* 2005; Gutiérrez *et al.* 2008; Parise 2019). The fractured formations of BF and SK were imaged by 2-D reflection seismic profiles (Wadas *et al.* 2016, 2017, 2018) and were also identified by outcrop investigations (Schmidt *et al.* 2013). The overburden in the two study areas is thin with only *ca*. 2 m (BF) to 60 m (SK) thickness, and the presence of cavities in the near surface was proven by inspection of core material (Schmidt *et al.* 2013). Altogether, the cavities and fractures result to high porosity and low density, not only in the subsurface erosion horizon, but also in the overlying material due to upward migrating fractures and cavities (Wadas *et al.* 2018). When a shear wave propagates through such material of low density and reduced shear strength, the wave velocity lowers. Similar observations were found by Uhlemann *et al.* (2016) for landslides, where the lowest *P*- and *S*-wave seismic velocities were found in the flow- and rotation-dominant domains of landslides, which are characterized by disturbed and deformed layers with presumably high porosity and low density. The two study areas BF and SK show different shear wave velocities for the low velocity zones within the subsurface erosion horizons. The low velocity zones in SK are characterized by velocities of around 200 to 350 m s^{-1} and in BF 120 to 300 m s^{-1} are observed. The lower velocities in BF indicate a more disturbed underground due to subsurface erosion compared to SK, which is evidenced by the core inspection, and the occurrence of much more sinkholes and depressions.

5.2 S-to-P-wave conversion

Other velocity anomalies observed in the data are relatively high V_S values that are physically inconsistent, because a shear wave is always slower than a compressional wave according to the wave theory. The particle motions of compressional waves are in the direction of propagation, mainly controlled by the compression modulus, and the less compressible the material the higher is the *P*-wave velocity, for example solid rocks show a higher *P*-wave velocity than sediments. The particle motions of shear waves on the other hand are perpendicular to the direction of wave propagation, only controlled by the shear modulus, which hampers energy propagation, and therefore slows down the wave velocity (Lowrie 2007). This velocity anomaly of too high V_S values indicates *S*-to-*P*-wave conversion. Wave conversion phenomena have been observed and investigated for seismic waves travelling through the Earth's crust, the lithosphere and the mantle (Bath & Stefansson 1966). Seismic investigations of the near-surface that deal with wave conversion are not so common, and the phenomenon of *S*-to-*P* conversion has rarely been studied. In theory, a plain S_H-wave can only be reflected and refracted as a S_H-wave and cannot be converted, as it is the case for *P* and S_V waves. Mi *et al.* (2015) studied shallow shear wave refraction seismic surveys and occurring S_H-wave conversions using numerical simulations. They state that an S_H wave can experience conversion in areas with non-horizontal or inhomogeneous layers, and this was also observed by Xia *et al.* (2002). Both state that in a subsurface with a dipping layer, when the seismic line is not perpendicular to the strata of the dipping surface, the incident S_H wave converts into a *P* wave. Since dipping surfaces in the subsurface of sinkhole areas are common, wave-type conversion is very likely.

Other studies discussed the influence of fractures on *S*-to-*P*-wave conversion. Nakagawa *et al.* (2000) investigated the interaction between seismic wave propagation and sheared fractures experimentally, numerically and analytically. They discovered that sheared fractures in a rock initiate conversion of the incident wave due to changes in fracture geometry, which leads to dilation behaviour of the fracture. It is described as shear-induced conversion of seismic waves. Another study was carried out by Bobet *et al.* (2017), who postulate that *S*-to-*P* conversion occurs due to the presence of an oriented microcrack network (or in our case a fracture network) that dilates under shear stress and causes shear wave splitting into *P*, *S* and *P*-to-*S* or *S*-to-*P* waves. Since both, dipping layers and dense fracture networks are found in our study areas in the subsurface erosion horizon as well as in the overlying material, we assume that a combination of both controls the observed *S*-to-*P* wave conversion. For a more detailed analysis of this phenomenon, regarding the identification of subsurface erosion induced unstable zones, FD modelling and other numerical approaches should be applied to synthetic and real data, like the data presented in this study.

5.3 Shear modulus and Poisson's ratio to determine ground stability

The seismic velocities were used to calculate the shear modulus μ and the Poisson's ratio νversus Shear modulus and Poisson's ratio are used in geotechnical engineering and describe the stiffness of a material, and therefore ground stability. The spatial distribution of μ of the presented data is similar to the spatial V_S distribution (Fig. 8), because the velocity values are squared for calculation of μ, in contrast to the density values. In general μ ranges between 80 and 8000 MPa for the VSPs, and 25 to 800 MPa for the 2-D profiles. The low-velocity zones of V_S, especially in the 2-D sections, result in low shear strength values between 25 and 250 MPa, which indicate an unstable subsurface. One such anomaly is observed for profile 3, which is located at the subsurface erosion induced leaning church tower of BF. μ shows severely reduced values below the leaning tower of around 25 MPa to 100 MP (Fig. 8.3c) and the core analysis of BF 01-2014 revealed a subsurface erosion induced decrease of the density of the Zechstein deposits, strong fracturing, and several small cavities in this depth (Wadas *et al.* 2016). Such low shear strength indicates a highly unstable subsurface, but the study areas show different shear modulus values depending on the degree of shear strength reduction. The subsurface erosion horizon around the urban sinkhole of SK (profiles 1 and 2) are characterized by μ values between 75 MPa to 250 MPa, whereas for profile 3 in the town of BF (south of the KSMF) μ ranges between 25 MPa and 100 MPa indicating a more unstable subsurface. Since the area north of the KSMF is less affected by subsurface erosion (Richter & Bernburg 1955) profile 4 displays higher μ values between 50 MPa and 250 MPa for the subsurface erosion horizon.

Indications of unstable zones can also be observed for the Poisson's ratio of the VSPs, which show ν values between 0.38 and 0.48, because gypsum, anhydrite and carbonate are affected by subsurface erosion and the overlying material is affected by fracture propagation. The high Poisson's ratio is also an indicator of reduced ground stability. Such characteristics for subsurface erosion areas were also observed by Uhlemann *et al.* (2016) for landslide investigations, and by Heap & Faulkner (2008) and Heap *et al.* (2009) for crack damage investigations during cyclic stressing of granite and basalt. Uhlemann *et al.* (2016) discovered that the translation-dominant domain of a landslide has a high Poisson's ratio of >0.40 due to saturated clay and sand, which indicates an increase in moisture content and perhaps porosity. They also assume that reactivation of landslide movement is a result of intense rainfall, therefore areas with a high Poisson's ratio might have a potential risk of future landslides. Heap & Faulkner (2008) and Heap *et al.* (2009) discovered that the Poisson's ratio increases with increased stress due to enhanced crack damage and fracture initiation. All these studies show the correlation of high or increased ν with possibly unstable zones, similar to the results of this work, which in contrast deals with subsurface erosion and the resulting structures.

5.4 Seismic attribute analysis to describe critical parameters

The seismic attribute analysis revealed strong attenuation of high frequencies and low similarity of adjacent traces, which correlate with the degree of subsurface erosion induced disturbance of the underground. Both are a direct result of the presence of fractures and intraformational faults due to mass-movement induced by subsurface erosion. Therefore, similarity and frequency are especially suited to detect and quantify lateral changes and heterogeneities in the subsurface and can be used to define critical parameters regarding ground stability. Based on the results of this study low frequencies between 20 and 55 Hz in combination with low similarities between 0.0 and 0.5 indicate highly unstable areas (Fig. 9). Both study areas show a similar frequency attenuation, but for BF a lower similarity is observed compared to SK. This correlates with the degree of subsurface erosion induced disturbance of the underground, which is more intense in BF, and anhydrite and gypsum are much shallower (Wadas *et al.* 2016) compared to SK (Wadas *et al.* 2017). Additionally, in BF brine production is still ongoing, which probably enhances the natural processes and the resulting subsurfaces disturbances.

So far, seismic attribute analysis have been mostly carried out for exploration-, reservoir- and geothermal studies, but not for sinkhole investigations. In such studies attributes like dip, azimuth, displacement and curvature are used for fault analysis (Lohr *et al.* 2008). These could also be used on a smaller scale for sinkhole investigations, because fault geometry and fault interaction play an important role in sinkhole formation (Delle Rose & Parise 2002; Abelson *et al.* 2003; Closson & Abou Karaki 2009; Pepe & Parise 2014; Wadas *et al.* 2017). Other studies successfully used, for example horizon-bound RMS (root mean square) variance amplitudes for the identification of subsurface structures (Buness *et al.* 2014), coherency as a valuable tool for structural analysis and the detection of unstable regions of oil fields (Maleki *et al.* 2015), spectral decomposition for the investigation of structurally complex carbonate platforms (von Hartmann *et al.* 2012), or instantaneous frequency for identification of fractured areas for geothermal exploration (Pussak *et al.* 2014). According to the study presented here, similarity/coherency is especially suited to detect and quantify lateral changes and heterogeneities in the subsurface, but further investigations should be carried out using, for instance spectral decomposition. The seismic attribute analysis can be further expanded by application on a 3-D seismic data set of a sinkhole.

6 SUMMARY AND CONCLUSIONS

Subsurface erosion areas are associated with structures such as sinkholes, caves, ground subsidence and springs. All these features represent difficult ground conditions for engineering and construction (Milanovic 2002; Parise *et al.* 2015), and pose a geohazard in urban areas. For the characterization of mechanical properties in regions affected by near-surface dissolution of soluble rocks, several VSPs, well logs and 2-D shear wave reflection seismic profiles were conducted. V_P and V_S were used to calculate the Poisson's ratio (ν) and the dynamic shear modulus (μ). Low shear wave velocity zones (V_S ranges from 120 to 350 m s^{-1} for the VSPs and from 200 to 400 m s^{-1} for the 2-D profiles) were identified in the subsurface erosion horizon and the disturbed overlying deposits. These zones result from a delay in seismic wave propagation due to fracture initiation and upward migrating fractures and cavities, which increase porosity and decrease density and thus the shear strength. In the 2-D sections, we observe lateral changes of μ that correlate with subsurface erosion induced structures located in the subsurface erosion horizon and the overlying material that are affected by fracture propagation and downbending of layers. These areas show low shear strength values between 25 and 250 MPa and are therefore characterized as unstable zones. Similar observations were made for the Poisson's ratio ν of the VSPs, which have high values of 0.38–0.48 for the presumed subsurface erosion horizon, and especially the disturbed overlying deposits. This is a further indicator

of reduced ground stability. Anomalies of μ and ν correlate with low electrical resistivities of less than 10 Ωm, which indicates high conductivity due to the presence of fluids and increased porosity. For the subsurface erosion horizon, a conversion of *S*-to-*P* wave is observed, which is probably a result of dipping layers and fracture networks. Seismic attribute analysis reveals strong attenuation of high frequencies and low similarity of adjacent traces, which correlate with the degree of subsurface erosion induced disturbance of the underground and this can be used to define critical parameters. Based on the results of this study, we suggest that low frequencies between 20 and 55 Hz, in combination with low similarities between 0.0 and 0.5, indicate highly unstable areas.

To conclude, site investigations using only borehole measurements will not be sufficient, because 1-D measurements are unable to detect lateral variations of rock properties that are typical for the disturbed underground of subsurface erosion areas. 2-D shear wave reflection seismic is ideally suited to depict these lateral changes. We propose the use of shear wave reflection seismic as a standard method, in combination with other geophysical techniques (e.g. gravimetry to detect cavities and mass movement (Neumann 1977; Butler 1984; Kobe *et al.* 2019), and electrical resistivity tomography (ERT) and various electromagnetic methods to identify fluid pathways and subsurface erosion areas (Militzer *et al.* 1979; Bosch & Müller 2005), for further investigation of sinkhole areas.

Further investigations should be carried out to understand the *S*-to-*P*-wave conversion (e.g. modelling approaches), the seismic attribute analysis (e.g. application of curvature or spectral decomposition to get more physical information about a subsurface erosion area), and the elastic moduli analysis of the shear modulus and the Poisson's ratio (e.g. application on a 3-D data set to get more spatial information on the distribution of the subsurface erosion horizon).

ACKNOWLEDGEMENTS

We are grateful for the valuable and constructive comments of three reviewers, Mario Parise and two anonymous referees. We also thank LIAG's seismic field crew for their excellent work during the surveys. We thank Hartwig von Hartmann from LIAG for helpful discussions about seismic attributes and we also thank David Tanner from LIAG for his help regarding the English. Furthermore, we thank the Thuringian State Institute for Environment, Mining and Conservation (Thüringer Landesamt für Umwelt, Bergbau und Naturschutz (TLUBN)) for supporting this work.

Author contribution statement: The seismic data was conducted by the first author together with the second and third co-authors, and LIAG's seismic field crew. Data processing, calculation and analysis of the seismic data was carried out by the first author. The first author created all figures and tables. Gamma ray and electrical resistivity of the boreholes were measured by section S5 'Borehole geophysics' of LIAG and were interpreted by the first author. The first author prepared and discussed the results with the co-authors. The first author wrote the paper and all co-authors inspired and helped to improve the manuscript, especially the discussion.

REFERENCES

Abelson, M., Baer, G., Shtivelman, V., Wachs, D., Raz, E., Crouvi, O., Kurzon, I. & Yechieli, Y., 2003. Collapse-sinkholes and radar interferometry reveal neotectonics concealed within the Dead Sea basin, *Geophys. Res. Lett.,* **30**(10), 52.1–52.3.

Al-Halbouni, D., Holohan, E.P., Taheri, A., Schöpfer, M.P.J., Emam, S. & Dahm, T., 2018. Geomechanical modelling of sinkhole development using distinct elements: model verification for a single void space and application to the Dead Sea area, *Solid Earth,* **9,** 1341–1373.

Al-Halbouni, D., Holohan, E.P., Taheri, A., Watson, R.A., Polom, U., Schöpfer, M.P.J., Emam, S. & Dahm, T., 2019. Distinct element geomechanical modelling of the formation of sinkhole clusters within large-scale karstic depressions, *Solid Earth,* **10,** 1219–1241.

Barnes, A.E., 2016. *Handbook of Poststack Seismic Attributes (Geophysical References),* Society of Exploration Geophysicists.

Bath, M. & Stefansson, R., 1966. S-P conversion at the base of the crust, *Ann. Geophys.,* **19**(2), 119–130.

Beutler, G. & Szulc, J., 1999. Die paläogeographische Entwicklung des Germanischen Beckens in der Trias und die Verbindung zur Tethys, in *Trias–Eine ganz andere Welt*, eds Hauschke N. & Wilde V., Dr. Friedrich Pfeil Scientific publisher.

Bobet, A., Modiriasari, A. & Pyrak-Nolte, S., 2017. Detection and monitoring of shear crack growth using S-P conversion of seismic waves, in *Proceedings of the AGU Fall Meeting 2017*, New Orleans, USA, 14 September 2017, https://agu.confex.com/agu/fm17/meetingapp.cgi/Paper/289061.

Bosch, F.P. & Müller, I., 2005. Improved karst exploration by VLF-EM-gradient survey: comparison with other geophysical methods, *Near Surf. Geophys.,* **3,** 299–310.

Brückl, E. *et al.*, 2005. Seismik, in *Handbuch zur Erkundung des Untergrundes von Deponien und Altlasten*, eds Knödel K., Krummel H. & Lange G., Springer-Verlag.

Bücking, H., 1906. *Geologische Karte von Preußen und benachbarten deutschen Ländern. Map Blatt Schmalkalden 5228, Preußische Geologische Landesanstalt,* Berlin, Germany.

Buness, H., von Hartmann, H., Rumpel, H.-M., Krawczyk, C.M. & Schulz, R., 2014. Fault imaging in sparsely sampled 3D seismic data using common-reflection-surface processing and attribute analysis–a study in the Upper Rhine Graben, *Geophys. Prospect.,* **62,** 443–452.

Butler, K., 1984. Microgravimetric and gravity gradient techniques for detection of subsurface cavities, *Geophysics,* **49**(7), 1084–1096.

Chopra, S. & Marfurt, K.J., 2007. *Seismic Attributes for Prospect Identification and Reservoir Characterization (Geophysical Developments No. 11),* Society of Exploration Geophysicists.

Ciccotti, M. & Mulargia, F., 2004. Differences between static and dynamic elastic moduli of a typical seismogenic rock, *Geophys. J. Int.,* **157,** 474–477.

Clayton, C.R.I., 2011. Stiffness at small strain: research and practice, *Géotechnique,* **61,** 5–37.

Closson, D. & Abou Karaki, N., 2009. Salt karst and tectonics: sinkholes development along tension cracks between parallel strike-slip faults, Dead Sea, Jordan, *Earth Surf. Process. Landforms,* **34,** 1408–1421.

Das, B.M., 2008. *Advanced Soil Mechanics,* 3rd edn, Taylor & Francis.

Delle Rose, M. & Parise, M., 2002. Karst subsidence in South-Central Apulia, Southern Italy, *Int. J. Speleol.,* **31,** 181–199.

dGB Beheer, B.V., 2017. *dGB Earth Sciences - OpendTect User Documentation - 6.0, dGB Beheer B.V.,* Enschede, Netherlands, http://static.dgbes.com/images/PDF/od_userdoc6.0.pdf.

Dittrich, E., 1966. Einige Bemerkungen über Rand- und Schwellenausbildungen im Zechstein Südwest-Thüringens, *Bericht der deutsch. Gesellsch. f. geolog. Wiss.,* **11,** 185–198.

Dreybrodt, W., 2004. Dissolution: evaporite rocks, in *Encyclopedia of Caves and Karst Science*, ed. Gunn J., Taylor & Francis Books.

Fahlman, B.D., 2011. *Materials Chemistry,* Springer-Verlag.

Freyberg, B.V., 1923. *Die tertiären Landoberflächen in Thüringen. Fortschritte der Geologie und Paläontologie Vol. 6,* Gebrüder Bornträger Verlag.

Giannakopoulos, A.E. & Suresh, S., 1997. Indentation of solids with gradients in elastic properties, *Int. J. Solids Struct.,* **34,** 2393–2428.

Goodman, R.E., 1989. *Introduction to Rock Mechanics,* John Wiley & Sons.

Grelle, G. & Guadagno, F.M., 2009. Seismic refraction methodology for groundwater level determination: 'water seismic index', *J. appl. Geophys.,* **68,** 301–320.

Griffiths, D.V. & Lane, P.A., 1999. Slope stability analysis by finite elements, *Géotechnique,* **49,** 387–403.

Gutiérrez, F., 2010. Chapter 13: Hazards associated with karst, in *Geomorphological Hazards and Disaster Prevention*, eds Alcantara-Ayala I., Goudie A.S., Cambridge Univ. Press.

Gutiérrez, F., Guerrero, J. & Lucha, P., 2008. A genetic classification of sinkholes illustrated from evaporite paleokarst exposures in Spain, *Environ. Geol.,* **53**(5), 993–1006.

Gutiérrez, F., Parise, M., De Waele, J. & Jourde, H., 2014. A review on natural and human-induced geohazards and impacts in karst, *Earth-Sci. Rev.,* **138,** 61–88.

Heap, M.J. & Faulkner, D.R., 2008. Quantifying the evolution of static elastic properties as crystalline rock approaches failure, *Int. J. Rock Mech. Min. Sci.,* **45,** 564–573.

Heap, M.J., Vinciguerra, S. & Meredith, P.G., 2009. The evolution of elastic moduli with increasing crack damage during cyclic stressing of a basalt from Mt. Etna volcano, *Tectonophysics,* **471,** 153–160.

Heap, M.J., Faulkner, D.R., Meredith, P.G. & Vinciguerra, S., 2010. Elastic moduli evolution and accompanying stress changes with increasing crack damage: implications for stress changes around fault zones and volcanoes during deformation, *Geophys. J. Int.,* **183,** 225–236.

Jaeger, J.C., Cook, N.G.W. & Zimmermann, R.W., 2007. Sinkholes in Evaporite Rocks, *Am. Sci.,* **86**(1), 38–51.

Johnson, K., 2005. Subsidence hazards due to evaporite dissolution in the United States, *Environ. Geol.,* **48,** 395–409.

Kobe, M., Gabriel, G., Weise, A. & Vogel, D., 2019. Time-lapse gravity and levelling surveys reveal mass loss and ongoing subsidence in the urban subrosion-prone area of Bad Frankenhausen, Germany, *Solid Earth,* **10,** 599–619.

Kowalski, W.C., 1991. Engineering geological aspects of different types of karst corrosion and fracture generation in karst masses, *Bull. Int. Assoc. Eng. Geol.,* **44,** 35–46.

Krawczyk, C.M., Polom, U., Trabs, S. & Dahm, T., 2012. Sinkholes in the city of Hamburg-New urban shear-wave reflection seismic system enables high-resolution imaging of subrosion structures, *J. appl. Geophys.,* **78,** 133–143.

Lacroix, P. & Amitrano, D., 2013. Long-term dynamics of rockslides and damage propagation inferred from mechanical modeling, *J. geophys. Res.,* **118,** 2292–2307.

Lerouiel, S., 2001. Natural slopes and cuts: movement and failure mechanisms, *Géotechnique,* **51,** 197–243.

Liu, H., 2017. *Principles and Applications of Well Logging,* Springer-Verlag.

Lohr, T., Krawczyk, C.M., Oncken, O. & Tanner, D.C., 2008. Evolution of a fault surface from 3D attribute analysis and displacement measurements, *J. Struct. Geol.,* **30,** 690–700.

Lowrie, W., 2007. *Fundamentals of Geophysics,* 2nd edn, Cambridge Univ. Press.

Maleki, S., Ramazi, H.R., Gholami, R. & Sadeghzadeh, F., 2015. Application of seismic attributes in structural study and fracture analysis of DQ oil field, Iran, *Egypt. J. Petrol.,* **24,** 119–130.

Mavko, G., Mukerji, T. & Dvorkin, J., 2009. *The Rock Physics Handbook Tools for Seismic Analysis of Porous Media,* Cambridge Univ. Press.

Mi, B., Xia, J. & Xu, Y., 2015. Finite-difference modeling of SH-wave conversions in shallow shear-wave refraction surveying, *J. appl. Geophys.,* **119,** 71–78.

Milanovic, P., 2002. The environmental impacts of human activities and engineering constructions in karst regions, *Episodes,* **25**(1), 13–21.

Militzer, H., Rösler, R. & Lösch, W., 1979. Theoretical and experimental investigations for cavity research with geoelectrical resistivity methods, *Geophys. Prospect.,* **27**(3), 640–652.

Mogi, K., 2007. Experimental rock mechanics, *Geomech. Res. Ser.,* **3,** 1–361.

Nakagawa, S., Nihei, K.T. & Myer, L.R., 2000. Shear-induced conversion of seismic waves across single fractures, *Int. J. Rock Mech. Min.,* **37,** 203–218.

Neumann, R., 1977, Microgravity method applied to the detection of cavities, in *Proceedings of the Symposium on Detection of Subsurface Cavities,* Vicksburg, MI, USA.

O'Connor, K.M. & Murphy, E.W., 1997. TDR monitoring as a component of subsidence risk assessment over abandoned mines, *Int. J. Rock Mech. Min.,* **34,** 3–4.

Parise, M., 2010. Hazards in Karst, in *Proceedings of the 'Sustainability of the Karst Environment. Dinaric Karst and other Karst Regions', Series on Groundwater,* **Vol. 2,** ed. Bonacci, O., pp. 155–162, https://www.researchgate.net/publication/281392130_Hazards_in_karst.

Parise, M., 2019, Sinkholes, in *Encyclopedia of Caves,* 3rd edn, Chapter 110, eds White, W.B., Culber, D.C. & Pipan, T., Academic Press.

Parise, M., Closson, D., Gutiérrez, F. & Stevanovic, Z., 2015. Anticipating and managing engineering problems in the complex karst environment, *Environ. Earth Sci.,* **74**(12), 7823–7835.

Pasquet, S., Bodet, L., Dhemaied, A., Mouhri, A., Vitale, Q., Rejiba, F., Flipo, N. & Guérin, R., 2015. Detecting different water table levels in a shallow aquifer with combined P-, surface and SH-wave surveys: insights from VP/VS or Poisson's ratios, *J. appl. Geophys.,* **113,** 38–50.

Pazzi, V., Morelli, S. & Fanti, R., 2019. A review of the advantages and limitations of geophysical investigations in landslide studies, *Int. J. Geophys.,* **4,** 1–27.

Pepe, M. & Parise, M., 2014. Structural control on development of karst landscape in the Salento Peninsula (Apulia, SE Italy), *Acta Carsol.,* **43**(1), 101–114.

Polom, U., Hansen, L., Sauvin, G., L'Heureux, J.-S., Lecomte, I., Krawcyzk, C.M., Vanneste, M. & Longva, O., 2010. High-resolution SH-wave seismic reflection for characterization of onshore ground conditions in the Trondheim Harbor, Central Norway, in *Advances in Near-Surface Seismology and Ground-penetrating Radar*, eds Miller R.D., Bradford J. & Holliger K., Wiley-Blackwell.

Pussak, M., Bauer, K., Stiller, M. & Bujakowski, W., 2014. Improved 3D seismic attribute mapping by CRS stacking instead of NMO stacking: application to a geothermal reservoir in the Polish Basin, *J. appl. Geophys.,* **103,** 186–198.

Richter, B. & Bernburg, G., 1955. Stratigraphische Gliederung des deutschen Zechsteins, *Zeitschr. Deutsch. Geol. Gesell.,* **105,** 843–854.

Schmidt, S., Wunderlich, J., Peters, A. & Heinke, O., 2013. Ergebnisbericht Ingenieurgeologische Erkundung des Erdfalls vom 01. November 2010 am Rötbergrain in Schmalkalden und Beschreibung des Erdfall Frühwarnsystems, Unpublished Report – Thuringian State Institute for Environment and Geology, pp. 1–179, Weimar, Germany.

Schneider-Löbens, C., Wuttke, M., Backers, T. & Krawczyk, C.M., 2015. Numerical modeling approach of sinkhole propagation using the eXtended FEM code roxol, in *Proceedings of the EGU General Assembly 2015* , Vienna, http://meetingorganizer.copernicus.org/EGU2015/EGU2015-12230-2.pdf, 2015 (last access: 13 September 2017).

Schriel, W. & Bülow, K.V., 1926a,b. Geologische Karte von Preußen und benachbarten deutschen Ländern. Map Frankenhausen 4632 and Map Kelbra 4532, Lieferung 9, 2. Auflage, Preußische Geologische Landesanstalt, Berlin, Germany.

Seidel, G., 2003. Geologie von Thüringen, Schweizerbart'sche Verlagsbuchhandlung, Stuttgart, Germany.

Simm, R. & Bacon, M., 2014. *Seismic Amplitude: An Interpreter's Handbook,* Cambridge Univ. Press.

Uhlemann, S., Hagedorn, S., Dashwood, B., Maurer, H., Gunn, G., Dijkstra, T. & Chambers, J., 2016. Landslide characterization using P- and S-wave seismic refraction tomography – the importance of elastic moduli, *J. appl. Geophys.,* **134,** 64–76.

von Hartmann, H., Buness, H., Krawczyk, C.M. & Schulz, R., 2012. 3-D seismic analysis of a carbonate platform in the Molasse Basin - reef distribution and internal separation with seismic attributes, *Tectonophysics,* **572–573,** 16–25.

Wadas, S.H., Polom, U. & Krawczyk, C.M., 2016. High-resolution shear-wave seismic reflection as a tool to image near-surface subrosion structures–a case study in Bad Frankenhausen, Germany, *Solid Earth,* **7,** 1491–1508.

Wadas, S.H., Tanner, D.C., Polom, U. & Krawczyk, C.M., 2017. Structural analysis of S-wave seismics around an urban sinkhole; evidence of en-

hanced dissolution in a strike-slip fault zone, *Nat. Hazard Earth Sys.,* **17,** 2335–2350.

Wadas, S.H., Tschache, S., Polom, U. & Krawczyk, C.M., 2018. Sinkhole imaging and identification of fractures with S_H-wave reflection seismic, in *Proceedings of the 15th Multidisciplinary Conference on Sinkholes and the Engineering and Environmental Impacts of Karst and the 3rd Appalachian Karst Symposium,* University of South Florida, FL, pp. 307–314.

Waltham, T., 2002. The engineering classification of Karst with respect to the role and influence of caves, *Int. J. Speleol.,* **31,** 19–35.

Waltham, T., Bell, F.G. & Culshaw, M., 2005. *Sinkholes and Subsidence-Karst and Cavernous Rocks in Engineering and Construction,* Springer-Verlag.

Xia, J., Miller, R.D., Park, C.B., Wightman, E. & Nigbor, R., 2002. A pitfall in shallow shear-wave refraction surveying, *J. appl. Geophys.,* **51,** 1–9.